Journal of Materials Chemistry C

ROYAL SOCIETY OF CHEMISTRY

PAPER

View Article Online
View Journal | View Issue

Cite this: J. Mater. Chem. C, 2025, 13, 21528

Molecular engineering, synthesis, and atomistic structure–property relationship of indoloquinoxaline-capped small donors for efficient organic solar cells

Maryam Javed,[a] Waqas Akram,[ab] Zeeshan Ali,[a] Nabeel Shahzad,[c] Munazza Shahid,*[d] Ghayoor Abbas Chotana,[e] Jafar Iqbal Khan,[f] Jie Min,[g] Muhammad Altaf,[a] Christian B. Nielsen*[h] and Raja Shahid Ashraf*[a]

Received 15th June 2025,
Accepted 18th August 2025

DOI: 10.1039/d5tc02318a

rsc.li/materials-c

The growing demand for high-performance organic photovoltaics has sparked great interest in small-molecule donor (SMD) materials that offer well-defined structures and superior batch-to-batch consistency. In this study, we report the molecular design, synthesis, and atomistic structure–property characterization of three indoloquinoxaline (IQ)-capped SMDs named **DPP-Th-IQ**, **BT-Th-IQ**, and **TT-IQ** for potential applications in all-small-molecule organic solar cells (ASM-OSCs). Each SMD features a distinct central core, including diketopyrrolopyrrole (DPP), benzothiadiazole (BT), or thieno[3,2-*b*]thiophene (TT) with thiophene as bridging units in the DPP and BT derivatives, to systematically tune electronic structures, optical profiles, and charge transport properties. Electrochemical analysis confirmed that all three SMDs possess well-aligned HOMO–LUMO levels conducive to pairing with the **Y6** non-fullerene acceptor. Density functional theory (DFT) calculations revealed low hole/electron reorganization energies with extensive frontier-orbital delocalization, indicative of efficient charge transport. Photophysical experiments based on UV-vis, photoluminescence, and solvatochromic analysis and complementary computational characterization showed strong intramolecular charge transfer in SMDs. Electron density difference analysis explained that particularly the benzothiadiazole-based **BT-Th-IQ** donor exhibits the lowest exciton binding energy coupled with high charge transfer excitations, indicating efficient exciton dissociation. Donor–acceptor interfacial modeling further predicted robust face-on π–π stacking and favorable donor-**Y6** orientations that support interfacial charge transfer. Importantly, all three SMDs demonstrated initial thin-film stability: films retained ≥90% of their initial absorbance after 30 hours of continuous AM 1.5G irradiation, and thermogravimetric analysis showed decomposition temperatures (5% weight loss) exceeding 250 °C. Overall, this study clarifies the interplay between molecular design, electronic structure, interfacial interactions, and stability, providing a strategic path toward next-generation high-efficiency ASM-OSCs based on IQ-capped donors.

1. Introduction

The continuously growing global demand for sustainable energy has accelerated research and development in advanced photovoltaic technologies. Among the various platforms, organic solar cells (OSCs) have garnered particular attention due to their potential for lightweight, flexible, and cost-effective energy harvesting devices. In contrast to certain hybrid perovskite and dye-sensitized solar cells that may employ toxic or corrosive materials, OSCs present a more environmentally benign alternative, relying on carbon-based materials with relatively lower toxicity profiles.[1–3] Early OSCs primarily utilized fullerene acceptors paired with small molecular donors, attaining modest yet promising power conversion efficiencies (PCEs).

[a] Department of Chemistry, Institute of Chemical Sciences, Government College University Lahore, Punjab 54000, Pakistan. E-mail: rajashahid@gcu.edu.pk
[b] Department of Chemistry, University of Agriculture, Faisalabad, 38000, Pakistan
[c] Department of Chemistry, Government College University, Faisalabad 38000, Pakistan
[d] Department of Chemistry, University of Education, Bank Road Campus, Lahore, Punjab 54000, Pakistan. E-mail: munazza.shahid@ue.edu.pk
[e] Department of Chemistry and Chemical Engineering, Lahore University of Management Sciences, Lahore, Punjab 54792, Pakistan
[f] Department of Physics, School of Natural Sciences, University of Hull, Hull HU6 7RX, UK
[g] The Institute for Advanced Studies, Wuhan University, Wuhan 430072, China
[h] Department of Chemistry, School of Physical and Chemical Sciences, Queen Mary University of London, London E1 4NS, UK. E-mail: c.b.nielsen@qmul.ac.uk

However, limitations such as narrow absorption coefficients, constrained energy-level tunability, and suboptimal thermal stabilities restricted these devices to PCE values of about 13%.[4]

Subsequent developments focused on the integration of non-fullerene acceptors (NFAs), which helped push OSC efficiencies above 20%.[5,6] NFAs offer advantages such as wider absorption ranges, customizable bandgaps, and improved morphological stability. Yet, pairing NFAs with polymer-based donors introduces additional complexities, with most notably polydispersity and potential morphological instabilities that may limit device reproducibility and long-term performance. In response, small molecular donors (SMDs) have emerged as compelling alternatives, owing to their well-defined molecular structures, tunable electronic structures for optimal donor–acceptor alignment, and batch-to-batch consistency. Nonetheless, despite these attributes, all-small-molecule OSCs (ASM-OSCs) continue to trail polymer–NFA systems in terms of overall efficiency, with most reports hovering around 15–16% PCE.[7–9] This discrepancy underscores the need for new small molecular donor designs that not only rival polymer-based donors but also surpass existing challenges related to morphology, stability, and scalability.

Molecular design strategies for small-molecule donors often involve A–D–A or A–π–D–π–A backbones, where electron-rich (donor) and electron-deficient (acceptor) units are carefully arranged to optimize energy-level alignment and facilitate efficient charge transfer. Building blocks like benzo-[1,2-*b*:4,5-*b*′]dithiophene (BDT) have been widely adopted due to their planar geometry, which enhances molecular packing and charge mobility.[10] Early BDT-containing donors achieved moderate PCEs when combined with fullerene acceptors, while subsequent efforts pairing BDT-based donors with high-performance **Y6**-type NFAs have driven ASM-OSC efficiencies beyond 15%.[11–13] Other core motifs, such as naphtho[1,2-*b*:5,6-*b*′]dithiophene, porphyrins, and thienobenzo-dithiophene (TBD), extend the available chemical space, enabling systematic fine-tuning of optical properties and energy levels.[14–16] Although these structural innovations have improved ASM-OSC performance, several practical issues persist. For example, many small-molecule donors lack the favorable film-forming characteristics inherent to polymers, necessitating additional processing or post-treatment steps to achieve optimal domain sizes and morphologies in the active layer. Moreover, certain small-molecule donors are prone to crystallization or self-aggregation, which, if not properly controlled, can hinder charge transport and limit device reproducibility.

Despite the advancements, the morphology of ASM-OSCs remains difficult to control. Achieving a continuous, yet finely mixed donor–acceptor network typically demands post-treatments (*e.g.*, thermal or solvent vapor annealing) that may be unsuitable for large-scale manufacturing.[16] Moreover, the low viscosity of small-molecule solutions complicates large-area printing of photoactive layers, posing a hurdle for industrial fabrication. Finally, although polymer-based materials often show greater morphological stability, questions persist regarding the long-term reliability of fully small-molecule systems.[17] Systematic stability studies will be integral as the field advances. Therefore, ASM-OSCs remain in a stage of ongoing materials exploration and efficiency enhancement, and more comprehensive answers to existing challenges may only emerge as a wider variety of donor–acceptor combinations are investigated. Progress is particularly dependent on the careful molecular engineering of small-molecule donors and acceptors to optimize key photovoltaic parameters: open-circuit voltage (V_{OC}), short-circuit current density (J_{SC}), and fill factor (FF). Achieving V_{OC} values above 0.90 V requires precise control of the donor's highest occupied molecular orbital (HOMO) and the acceptor's lowest unoccupied molecular orbital (LUMO) energy levels, while broad absorption spectra and high charge-carrier mobility are essential to maximizing both J_{SC} and FF.[18–20] Consequently, the primary obstacle lies in designing donor–acceptor (D/A) systems with aligned energy levels, extended absorption across the visible to near-infrared region, and robust morphological and electronic properties. Addressing this challenge necessitates the discovery and development of efficient SMDs that not only meet these stringent performance criteria but also enhance device stability, thereby paving the way for future efficient ASM-OSCs.

This study reports the design, synthesis, and computational characterization of three new SMDs based on indoloquinoxaline (IQ) end-groups and two electron-deficient central cores, including diketopyrrolopyrrole (DPP), and benzothiadiazole (BT), one electron-rich core, thienothiophene (TT) and named as **DPP-Th-IQ**, **BT-Th-IQ**, and **TT-IQ**, respectively. IQ-based architecture has recently garnered increasing interest. The intrinsic donor–acceptor character of 6*H*-indolo[2,3-*b*]quinoxaline, which is derived from electron-rich indole ring and electron-deficient quinoxaline fragment facilitates efficient intramolecular charge transfer (ICT), making it a promising terminal unit in SMD design. Among central units, DPP stands out for its robust electron-transporting capacity, high photochemical stability, and strong absorption, whereas BT is a versatile acceptor fragment easily synthesized from readily available precursors. Both DPP- and BT-centered molecules are further modified with thiophene π-bridges to extend conjugation and fine-tune energy levels. By contrast, TT central unit imparts a rigid backbone that is conducive to planar packing and efficient π–π interactions, potentially boosting charge mobility and light absorption. By systematically examining the structural, optical, electrochemical, and charge transfer (CT) properties of these IQ-capped donors with distinct core units, we aim to clarify structure–property relationships at atomistic level and highlight promising design principles for next-generation ASM-OSCs.

2. Materials and methods

2.1. Materials and instruments

All reagents and catalysts were purchased from Sigma-Aldrich and Tokyo Chemical Industry and used without further purification. Solvents, including dichloromethane (DCM), ethyl acetate, and *n*-hexane, were procured from local vendors and

distilled prior to use. Melting points were determined using a Jindal melting point apparatus with open capillary tubes. ^{1}H and ^{13}C NMR spectra were recorded on a Bruker Ascend 400 MHz spectrometer, employing deuterated chloroform ($CDCl_3$) as the solvent and trimethylsilane (TMS) as an internal reference. The IR spectra were recorded using a Bruker Alpha Platinum ATR spectrometer. The UV-vis absorption spectra were obtained using a Shimadzu Pharmaspec UV-1700 spectrophotometer in both solutions and solid films and photoluminescence (PL) spectra were measured using a Cary Eclipse Fluorescence Spectrophotometer. Photostability tests were performed under continuous AM 1.5G illumination (100 mW cm^{-2}) using a G2V Optics Pico™ LED solar stimulator. PerkinElmer USA, model STA 8000 device was used to examine the stability of compounds at varied temperatures (20–120 °C). In a nitrogen atmosphere, at a heating rate of 10 °C min^{-1} thermogravimetric analysis (TGA) was performed in the temperature range of 30 °C to 700 °C. For cyclic voltammetry measurements, a standard three-electrode configuration was employed in a PalmSens EmStat3+ potentiostat, using Ag/AgCl as the reference electrode, fluorine-doped tin oxide (FTO) glass as the working electrode, and ferrocene as an internal reference.

2.2. Computational methodology

Density functional theory (DFT) and time-dependent DFT (TD-DFT) calculations were carried out with Gaussian 09 software.[21–24] B3LYP hybrid functional combined with the 6-31G(d,p) basis set was employed to model molecular geometries and electronic structures.[25,26] Vibrational frequency calculations were performed to confirm that all geometries correspond to local minima on the potential energy surface. For electronic structures, Mulliken population analysis was employed to investigate the contributions of individual molecular fragments to the frontier molecular orbitals (FMOs). Furthermore, the density of states (DOS) and partial density of states (PDOS) of the molecular units in the donors were analyzed using PyMOlyze-1.1 software.[27] The solvent-phase absorption spectra was simulated by CAM-B3LYP/6-31G(d,p) method with IEFPCM model and Gibbs solvation free energy (ΔG_{solv}) was simulated using the SMD model by M06-2X/6-31G(d,p) method.[28]

Electron density difference (EDD) analysis were conducted for every optimized SMD and SMD/acceptor complexes in order to visualize the redistribution of charge upon photo-excitation and to extract quantitative charge transfer descriptors.[21,29] Following Le Bahers *et al.* and the Multiwfn 3.8 implementation, four primary quantities given in eqn (1)–(4) were evaluated from the difference density $\Delta\rho(r) = \rho_{ele}(r) - \rho_{hole}(r)$:[21,30]

$$D_{CT} = |R_{ele} - R_{hole}|; \quad R_{ele/hole} = \frac{\int \rho_{ele/hole}(r) r \mathrm{d}r}{\int \rho_{ele/hole}(r) \mathrm{d}r} \tag{1}$$

$$q_{CT} = \frac{1}{2}\int |\rho_{ele}(r) - \rho_{hole}(r)| \mathrm{d}r \tag{2}$$

$$D_{index} = \frac{\sum_i \rho_{ele} i \rho_{hole} i |r_i - R_{hole}|}{\sum_i \rho_{ele} i \rho_{hole} i} \tag{3}$$

$$t_{index} = D_{CT} - H_{index} \tag{4}$$

where D_{CT} is the electron–hole centroid separation among the barycentre, q_{CT} the total transferred charge magnitude. Whereas, the indices H_{index}/t_{index} were used to evaluate charge transition behavior and the extent of charge separation. H_{index} is the spatial extent of the transition along the CT axis, and t_{index} is a separation metric that approaches zero when electron and hole strongly overlap. Through-space CT mechanism was examined based on these EDD parameters. In practice, higher D_{CT} together with large q_{CT} and low H_{index} is taken as an indicator of efficient spatial charge separation.

For each excited state the inter-fragment charge-transfer (IFCT) matrix was built and the relative contributions of charge-transfer and local excitations were obtained from eqn (5) and (6):

$$\mathrm{CT}\ (\%) = \frac{\sum_{D \neq A} q_{D \to A}}{\sum_{all} q_{i \to j}} \times 100 \tag{5}$$

$$\mathrm{LE}\ (\%) = 100 - \mathrm{CT}\ (\%) \tag{6}$$

where $q_{D \to A}$ is the electron population transferred from donor fragment D to acceptor fragment A.

A large D_{CT} or CT (%) combined with a small H_{index}, t_{index} and LE (%) evidences efficient charge separation and, by extension, a reduced probability of geminate and non-geminate recombination in organic photovoltaic materials. In addition, the transition density matrix (TDM) and hole/electron overlap heat maps were generated to visualize electron–hole coherence across molecular fragments in SMDs.[30,31] All EDD and IFCT quantities were obtained directly *via* Multiwfn 3.8 on excited-state wave-functions calculated using the range-separated hybrid (RSH) functional ''CAM-B3LYP''.[32–35]

The charge transport capabilities of the materials were assessed by calculating reorganization energy, a key parameter for estimating charge carrier mobility in organic materials. The adiabatic potential energy surface (PES) approach was used to compute the reorganizational energy of holes (λ_{hole}) and electrons (λ_{ele}), respectively.[36,37] These values were derived based on the relaxation of the cationic and anionic states to the neutral molecular geometry, as defined by the following eqn (7) and (8):

$$\lambda_{hole} = (E^{+}_{neutral} - E_{neutral}) + (E_{cationic} - E^{0}_{cationic}) \tag{7}$$

$$\lambda_{ele} = (E^{-}_{neutral} - E_{neutral}) + (E_{anionic} - E^{0}_{anionic}) \tag{8}$$

where, $E_{neutral}$ represents the neutral molecule energy, $E^{+}_{neutral}$ and $E^{-}_{neutral}$ are the cationic and anionic states energies optimized from the neutral geometry, while $E_{cationic}$ and $E_{cationic}$

denote the cationic and anionic states energies, respectively. Whereas, E^{0}_{cationic} and E^{0}_{anionic} correspond to the energy of the neutral molecule optimized in the cationic and anionic geometries, respectively.

3. Results and discussion

3.1. Synthesis

The synthesis of side-peripheral **IQ** groups was carried out with the preparation of 8-bromo-6*H*-indolo[2,3-*b*]quinoxaline derivatives *via* a straightforward condensation reaction, as previously described in the literature.[38] This involved the reaction of 1,2-diaminobenzene with 6-bromoindoline-2,3-dione in glacial acetic acid under reflux, yielding the target compound in a high yield of 87%. To improve the solubility and processability of the rigid-structured fused-ring **IQ** derivatives, *N*-alkylation was performed using 2-ethylhexyl bromide and potassium carbonate in dimethylformamide at 80 °C overnight, resulting in the formation of 8-bromo-6-(2-ethylhexyl)-6*H*-indolo[2,3-*b*]quinoxaline (**C$_8$IQa**). Subsequent borylation was carried out using bis(pinacolato)diboron as the borylating agent, in the presence of palladium acetate, X-Phos as the catalyst, and potassium acetate as the base, resulting in 6-(2-ethylhexyl)-8-(4,4,5,5-tetramethyl-1,3,2-dioxaborolan-2-yl)-6*H*-indolo[2,3-*b*]-quinoxaline (**C$_8$IQb**), as given in Scheme 1.

Small molecular donors with DPP, BT, and TT cores were synthesized with **IQ** moieties as terminal groups through different synthesis pathways. Thiophene was used as a bridging unit in the DPP- and BT-based donor derivatives, while the TT-based derivative synthesised without the bridging thiophene units, as illustrated in Scheme 1. The donor molecule 2,5-bis-(2-ethylhexyl)-3,6-bis(5-(6-(2-ethylhexyl)-6*H*-indolo[2,3-*b*]quinoxalin-8-yl)thiophen-2-yl)-2,5-dihydropyrrolo[3,4-*c*]pyrrole-1,4-dione (**DPP-Th-IQ**) was synthesized starting from 3,6-di(thiophen-2-yl)-2,5-dihydropyrrolo[3,4-*c*]pyrrole-1,4-dione. Initially, *N*-alkylation of the DPP core was achieved by reacting 2-ethylhexyl bromide with potassium carbonate in DMF at 80 °C for 24 hours, producing 2,5-bis(2-ethylhexyl)-3,6-di(thiophen-2-yl)-2,5-dihydropyrrolo[3,4-*c*]-pyrrole-1,4-dione. Bromination of this intermediate with *N*-bromosuccinimide (NBS) in DMF at 60 °C overnight yielded (**1**). Finally, the target **DPP-Th-IQ** donor was synthesized through Suzuki–Miyaura cross-coupling reaction between **1** and **C$_8$IQb** in the presence of a palladium catalyst, resulting in a 57% yield after purification. The BT-based donor, 4,7-bis(5-(6-(2-ethylhexyl)-6*H*-indolo[2,3-*b*]quinoxalin-8-yl)thiophen-2-yl)benzo[*c*][1,2,5]thiadiazole (**BT-Th-IQ**), was synthesized starting from 4,7-dibromobenzo[*c*]-[1,2,5]thiadiazole (DBBT). Initially, a Stille coupling reaction was

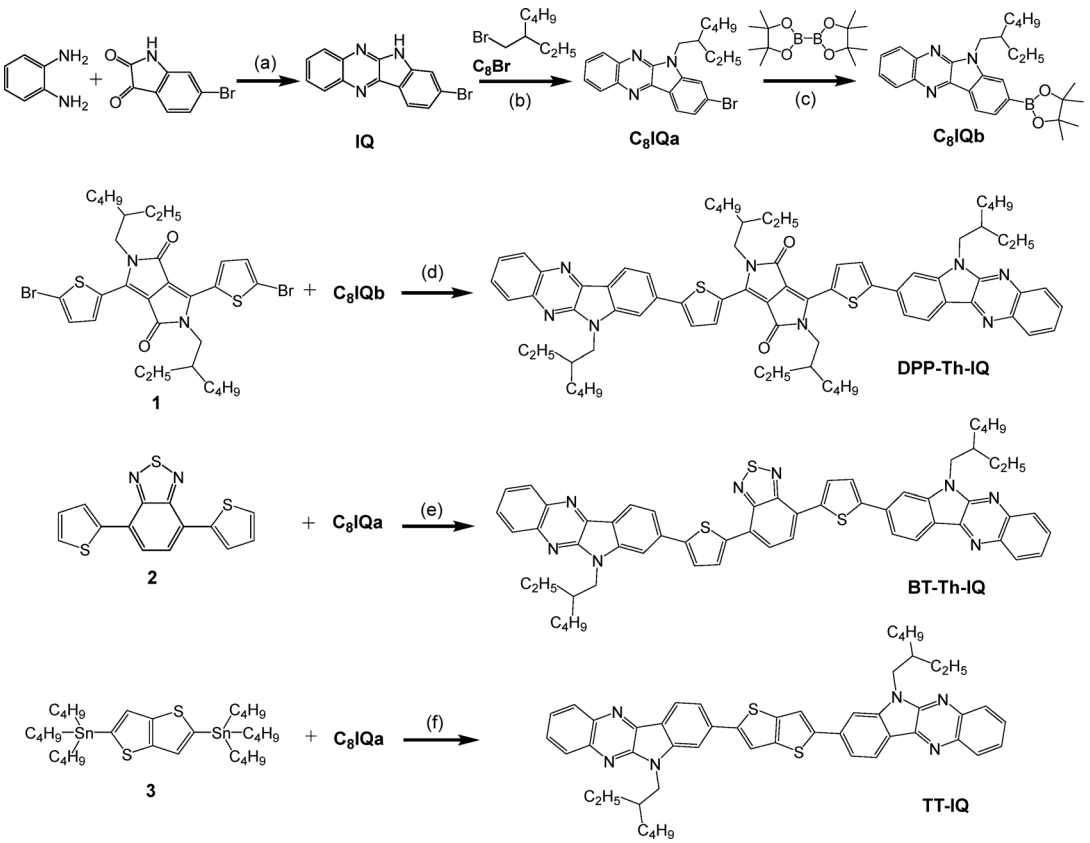

Scheme 1 Synthesis pathway of diketopyrrolopyrrole (DPP), benzothiadiazole (BT), and thieno[3,2-*b*]thiophene (TT) core units containing small molecular donors: (a) glacial acetic acid, DMF, reflux 24 h, (yield, 87%) (b) 2-ethylhexyl bromide, K_2CO_3, DMF, 85 °C, 18 h, (yield, 80%) (c) bis(pinacolato)diboron, $Pd(CH_3COO)_2$, X-Phos, CH_3CO_2K, toluene, 85 °C, 14 h (yield, 75%) (d) $Pd(CH_3COO)_2$, X-Phos, K_2CO_3, THF/water, 85 °C, 18 h (yield, 57%) (e) $Pd(CH_3COO)_2$, K_2CO_3, pivalic acid, $PCy_3{\cdot}HBF_4$ ligand, DMA, 110 °C, 5 h (yield, 78%) (f) $PdCl_2(PPh_3)_2$, THF, 65 °C, 24 h (yield, 87%).

performed between DBBT and tributyl(thiophen-2-yl)stannane in the presence of dichlorobis(triphenylphosphine)palladium(II) as the catalyst and tetrahydrofuran (THF) as the solvent, yielding (**2**). Direct arylation (C–H activation) of **2** with **C_8IQa** yielded the final **BT-Th-IQ** donor in a 78% yield. Whereas, the TT-based donor, 2,5-bis(6-(2-ethylhexyl)-6*H*-indolo[2,3-*b*]quinoxalin-8-yl)thieno[3,2-*b*]thiophene (**TT-IQ**), was synthesized in a single step *via* Stille coupling. This involved the reaction of 2,5-bis(tributylstannyl)thieno[3,2-*b*]thiophene (**3**) with the prepared brominated **IQ** derivative **C_8IQa** using dichlorobis(triphenylphosphine)palladium(II) as the catalyst in THF. The reaction afforded **TT-IQ** in high yield (87%) after purification. The chemical structures of synthesized intermediates and compounds were confirmed by ^{1}H NMR and ^{13}C NMR spectroscopy, and the corresponding spectra are provided in the SI (Fig. S1–S9), along with detailed reaction kinetics.

3.2. Energy levels and estimated driving-force offsets

An understanding of the HOMO and LUMO energies is paramount when designing efficient D/A systems for BHJ-OSCs. In particular, the donor's HOMO must be sufficiently deep to maximize the V_{OC} of OSCs, while the donor's LUMO should be higher than that of the acceptor to facilitate efficient electron transfer and prevent back-electron transfer.[39,40] Table 1 provides the electrochemical properties of the newly synthesized IQ-capped SMDs based on the CV experiments alongside the benchmark **Y6** NFA. For insights into the redox behavior and energy levels estimation of the synthesized SMDs, CV measurements were carried out in anhydrous dichloromethane (5 mL) containing 2 mM of the analyte and 0.1 M tetrabutylammonium hexafluorophosphate ($TBAPF_6$) as the supporting electrolyte, at a scan rate of 50 mV s^{-1}. The solutions were purged with dry N_2 for 5 min prior to measurements. Oxidation (E_{ox}^{onset}) and reduction (E_{red}^{onset}) onsets were referenced to the ferrocene/ferrocenium redox couple (Fc/Fc^+), assuming an absolute HOMO of 4.88 eV for Fc/Fc^+. CV profiles and an energy-level diagrams comparing SMDs to **Y6** are shown in Fig. 1a–d. Whereas, the CV profiles of the SMDs with the labelled oxidation and reduction potential values are given in the SI, Fig. S10a–c.

From the CV results, we inferred that **DPP-Th-IQ** exhibited an oxidation onset (E_{ox}) of approximately 1.05 V and a reduction onset (E_{red}) of −0.67 V, leading to a calculated HOMO energy (E_H) of −5.35 eV and LUMO energy (E_L) of −3.70 eV. The electrochemical bandgap (E_g^{CV}) was thus 1.65 eV, which is almost consistent with optical bandgap (E_g^{opt}) of 1.71 eV, **TT-IQ** showed a slightly lower oxidation potential but a more negative reduction potential of −0.87 V, indicative of the electron-rich thieno[3,2-*b*]thiophene core's influence on the redox behavior. The E_H and E_L were determined to be −5.30 eV and −3.44 eV, respectively, and the E_g^{CV} was observed as 1.86 eV. Whereas **BT-Th-IQ**, incorporating the electron rich BT fragment, exhibited the lowest oxidation onset at 0.91 V and a reduction onset of −0.95 V, resulting in E_H of −5.13 eV and E_L of −3.35 eV. While the E_g^{CV} of **BT-Th-IQ** SMD was estimated as 1.78 eV, almost consistent with the E_g^{opt} 1.85 eV based on the onset absorption spectra (Table 1). Small disparity in bandgaps reflect intra- and intermolecular interactions that shift the absorption edge in thin films. Overall, the deeper E_H (around −5.3 to −5.4 eV) of **DPP-Th-IQ** and **TT-IQ** suggest a higher attainable V_{OC} compared to **BT-Th-IQ**, yielding a shallower E_H (−5.13 eV) which could reduce the maximum achievable voltage in cell device. Meanwhile, all three SMDs have E_L well above that of **Y6** (−4.1 eV),[41] ensuring a sufficient offset for exciton dissociation at D/A interface as shown in Fig. 1c and d.

The V_{OC} was estimated by pairing the SMDs with benchmark **Y6** acceptor based on the Scharber relation, which incorporates the donor's E_H and the acceptor's E_L along with an empirical offset of 0.3 V for charge separation. Under these assumptions, **DPP-Th-IQ** and **TT-IQ** both resulted in relatively high predicted V_{OC} values of 0.95 and 0.90 V, respectively. By contrast, **BT-Th-IQ** exhibited a lower estimated V_{OC} of 0.73 V, owing to its upshifted HOMO and comparatively smaller HOMO–LUMO offset with **Y6**. Efficient exciton dissociation in OSCs typically requires a minimum energy offset of ∼0.2–0.3 eV between the donor and acceptor LUMOs (ΔE_{L-L}) and often an analogous offset in HOMOs (ΔE_{H-H}).[42] Here, all three SMDs demonstrated sufficient LUMO energy offsets with **Y6** NFA, such as **DPP-Th-IQ**, **BT-Th-IQ**, and **TT-IQ** showcased the offsets of 0.40 eV, 0.75 eV, and 0.66 eV, respectively. Although a larger offset favors electron transfer, it can also lead to energy losses that lower the V_{OC} as demonstrated in interfacial CT mechanism in Fig. 1b. This trade-off is exemplified by **BT-Th-IQ**, which has the

Table 1 Electronic structure parameters and energy-driving potential of designed DPP-, BT-, and TT-based donor molecules when blended against the benchmark **Y6** acceptor. The V_{OC} and driving-force offsets for **Y6** acceptor were evaluated against polymer donor PM6[41]

Molecule	E_H[a] (eV)	E_L[a] (eV)	E_g^{CV}[b] (eV)	E_g^{opt}[c] (eV)	V_{OC}[d] (V)	ΔE_{L-L}[e] (eV)	ΔE_{H-H}[e] (eV)
DPP-Th-IQ	−5.35	−3.70	1.65	1.71	0.95	0.4	0.35
BT-Th-IQ	−5.13	−3.35	1.78	1.85	0.73	0.75	0.57
TT-IQ	−5.30	−3.44	1.86	1.96	0.9	0.66	0.4
Y6	−5.65	−4.10	1.60	1.51	1.1	0.54	0.2

[a] HOMO and LUMO energy level (E_H and E_L, respectively) as determined by the oxidation (E_{ox}^{onset}) and reduction onsets (E_{red}^{onset}) by CV *via* relation $E_{HOMO} = -(E_{ox}^{onset} - E_{Fc}^{onset} + 4.8)$ eV and $E_{LUMO} = -(E_{red}^{onset} - E_{Fc}^{onset} + 4.8)$ eV. [b] Energy bandgap (E_g^{CV}) determined from the CV calculations *via* relation $E_g^{CV} = E_H - E_L$. [c] Energy bandgap (E_g^{opt}) determined by the onset spectra. [d] Open-circuit voltage (V_{OC}) evaluated *via* Scharber relation as $V_{OC} = \frac{E_{H(donor)} - E_{L(acceptor)}}{e} - 0.3$, where E_L is LUMO of acceptor, E_H is HOMO level of donor, e is the elementary charge, and 0.3 V is an empirical factor for charge separation. [e] ΔE_{L-L} is the energy difference between E_L of acceptor to E_L of the donor, while ΔE_{H-H} is the energy difference from E_H of acceptor to E_H of the donor.

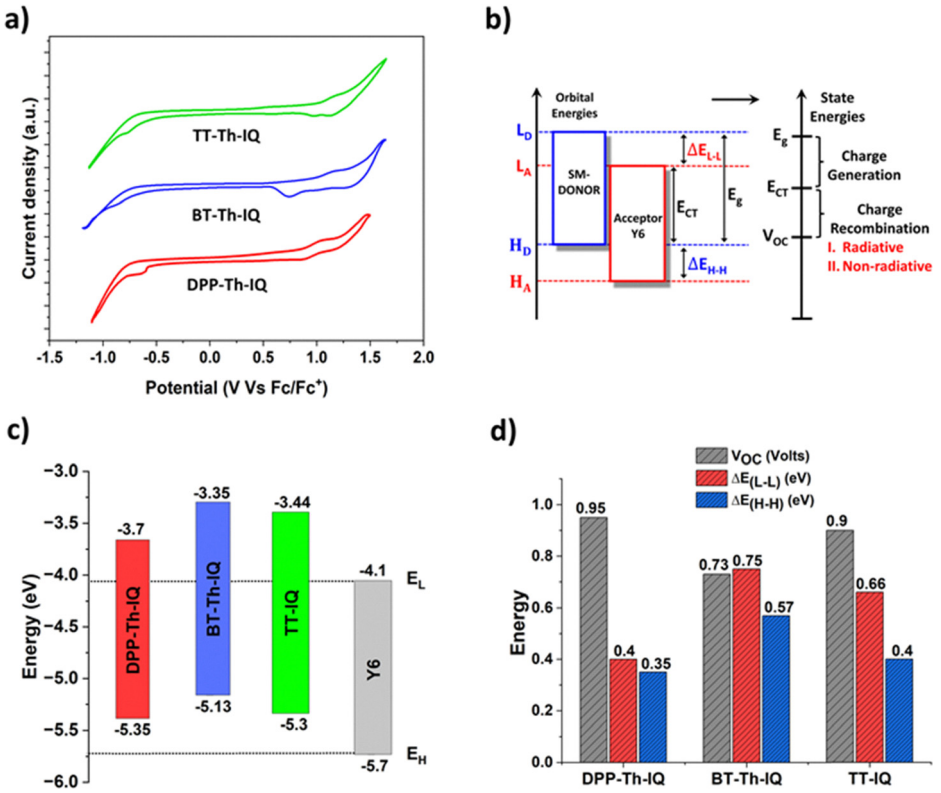

Fig. 1 Cyclic voltammograms of SMDs measured in anhydrous dichloromethane (5 mL) containing 2 mM of the analyte and 0.1 M tetrabutylammonium hexafluorophosphate ($TBAPF_6$) as the supporting electrolyte, at a scan rate of 50 mV s^{-1}. (b) Energy levels diagram representing HOMO/LUMO energy levels of donor (H_D/L_D) and HOMO/LUMO energy levels acceptor (H_A/L_A) for feasible charge transfer mechanism in photoactive configuration. (c) Energy levels diagram and (d) estimated open-circuit voltage (V_{OC}) based on Scharber relation with respective driving-force offsets of the SMDs against benchmark **Y6** NFA.

largest ΔE_{L-L} of 0.75 eV but the lowest predicted V_{OC} value of 0.73 V. In contrast, **DPP-Th-IQ** exhibited a balanced approach maintaining a sufficient LUMO offset of 0.40 eV for electron transfer while preserving a relatively high potential for V_{OC}. From device engineering perspective, the ideal D/A pair balances a minimal energy offset to reduce voltage losses with sufficient offset to drive exciton dissociation and minimize charge recombination. Thus, while **BT-Th-IQ** can provide robust electron-driving potential, its upshifted HOMO level poses a challenge for maximizing V_{OC}. Conversely, **DPP-Th-IQ** and **TT-IQ** exhibited deeper HOMOs with adequate LUMO offsets, indicating promise for higher V_{OC} alongside efficient charge generation.

3.3. Electronic structure properties

To elucidate how molecular geometry and electronic configuration influence the performance of the synthesized IQ-capped SMDs, DFT calculations were performed at B3LYP/6-31G(d,p) level of theory. Fig. 2a presents the optimized geometry, highlighting the dihedral angles between the IQ end-groups, any bridging thiophene rings, and the central cores. In **DPP-Th-IQ**, the IQ-thiophene and thiophene-DPP core dihedral angles are 25.2° and 11.1°, respectively. In **BT-Th-IQ**, the IQ-thiophene dihedral measures 25.7°, whereas the thiophene–BT core dihedral is 8.5°. Larger angels between side IQs and thiophene bridges are due to steric repulsions among neighboring hydrogen atoms of fused benzene IQ units and thiophenes. The **TT-IQ**, which lacks bridging thiophene rings, exhibited IQ-TT core dihedral of 26.1°. Overall, the SMDs exhibited quasi-coplanar arrangements which can partially reduce π-conjugation but geometry is sufficient for effective ICT and electronic delocalization.

Molecular electrostatic potential (MESP) maps given in Fig. 2b further revealed distinct regions of positive (blue) and negative (red) potential, corresponding to electron-deficient and electron-rich moieties, respectively.[43] Across the three SMDs, the electronegative atoms (nitrogen in IQ and sulfur in the core/thiophene) tend to attract electron density to produce negative potential localized pockets. Simultaneously, the alkyl-substituted fragments and less electronegative regions appeared as positive potential zones. This spatial variation in electrostatic potential not only corroborates the partial donor–acceptor character inherent to each molecule but also rationalize the observed CT pathways. Regions exhibiting strongly negative potential often overlap with segments that accept electron density in the LUMO, whereas areas of positive potential align with electron-rich sites in the HOMO and provide a complementary perspective on how holes/electrons may be distributed/transferred upon excitation.

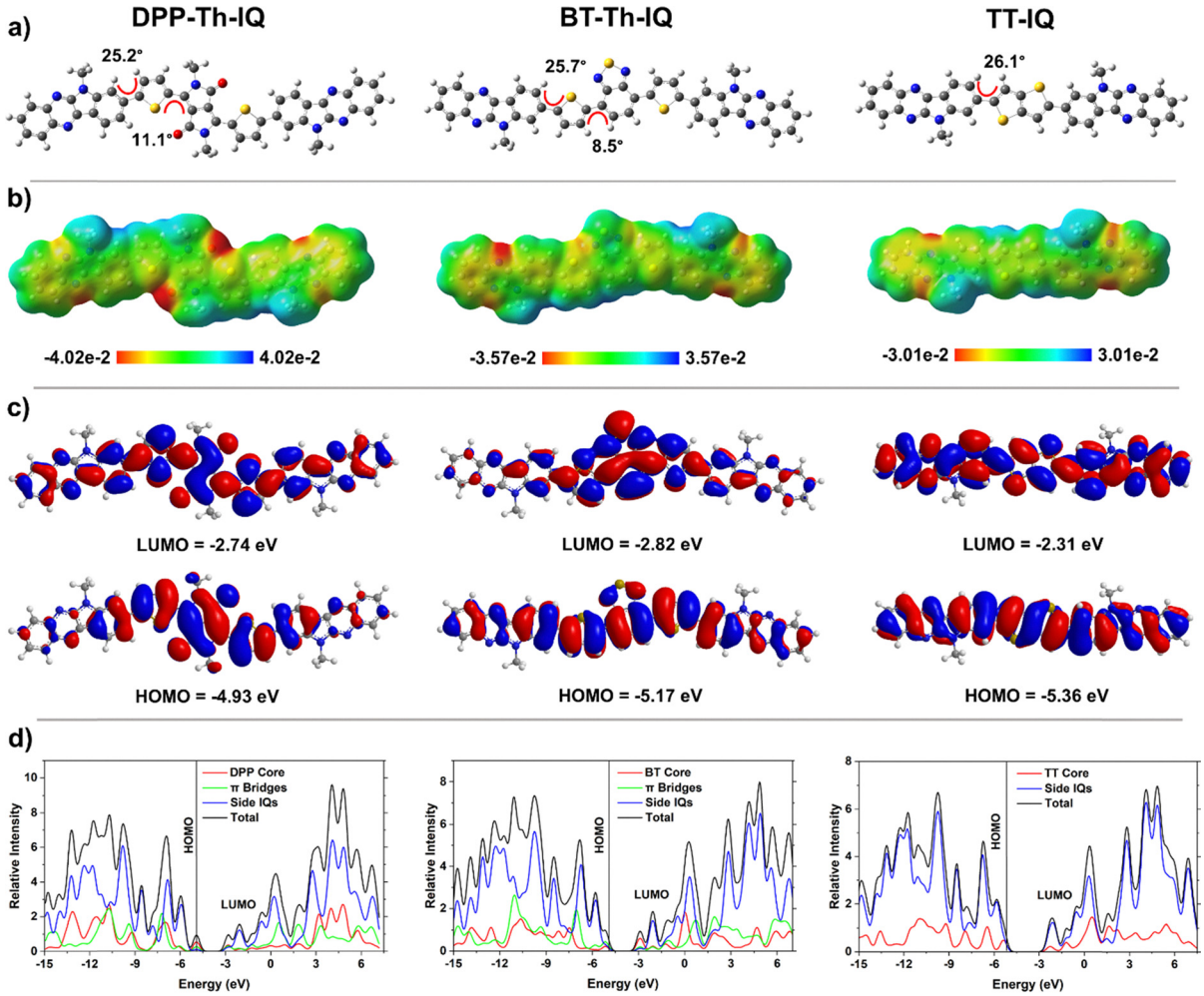

Fig. 2 (a) Optimized molecular geometries, (b) molecular electrostatic potential (MESP) surfaces, (c) frontier molecular orbitals delocalization, and (d) partial DOS (PDOS) graphs based on core, bridging, and end-capped fragments in the SMDs simulated by B3LYP/6-31G(d,p) method.

Furthermore, the FMOs analysis based on delocalization of HOMOs and LUMOs given in Fig. 2c and PDOS graphs based on Mulliken analysis in Fig. 2d showed that the HOMOs of **DPP-Th-IQ** and **TT-IQ** delocalize on electron-rich cores (≈58% for **DPP-Th-IQ** and ≈52% for **TT-IQ**). Whereas, the **BT-Th-IQ**'s HOMO is more evenly distributed between the core (≈25%) and thiophenes (≈49%). Such a broad HOMO delocalization can improve hole mobility, an essential feature for efficient donors in OSCs.[44,45] In contrast, the LUMOs of the SMDs exhibited varied localization. **BT-Th-IQ**'s LUMO (≈68%) on the core reflects the strong electron-withdrawing character of benzothiadiazole, while **TT-IQ**'s LUMO lies predominantly on the IQ end-groups (≈80%). **DPP-Th-IQ** displayed a more balanced LUMO distribution across the central DPP core, bridging thiophenes, and IQ terminal. These results are summarized in SI, Table S1. Although torsional angles introduce partial breaks in π-conjugation, the inherent donor–acceptor motif promotes a robust ICT pathway, as evidenced by the even frontier-orbital delocalization and PDOS patterns. Moreover, comparing the DFT-derived HOMO–LUMO gaps with experimentally measured electrochemical bandgaps (Table 1) shows consistent trends and validates the computational approach. Slight deviations are attributable to inherent DFT approximations and excitonic effects in the solid state. Overall, these findings underscore that a careful balance of backbone planarity, donor–acceptor segmentation, and electron-rich bridging motifs can be harnessed to fine-tune HOMO–LUMO energy levels, thereby enhancing both charge transport and device performance in OSCs.

3.4. Optical properties and solvatochromism

Optical characteristics of synthesized SMDs were evaluated to assess their suitability in OSCs. Table 3 summarizes the experimental absorption and emission spectral characteristics, along with respective theoretical parameters derived from TD-DFT calculations. Steady state optical spectroscopy was employed to examine the SMDs in dilute chloroform solutions (2.5 μg mL^{-1}). The UV-vis spectra of the representative samples are shown in Fig. 3a, with the absorption covering the spectral range of 500 nm, 570 nm and 740 nm. The latter sample exhibited extended absorption and broader spectrum compared to its counterparts. Whilst **TT-IQ** yielded an absorption

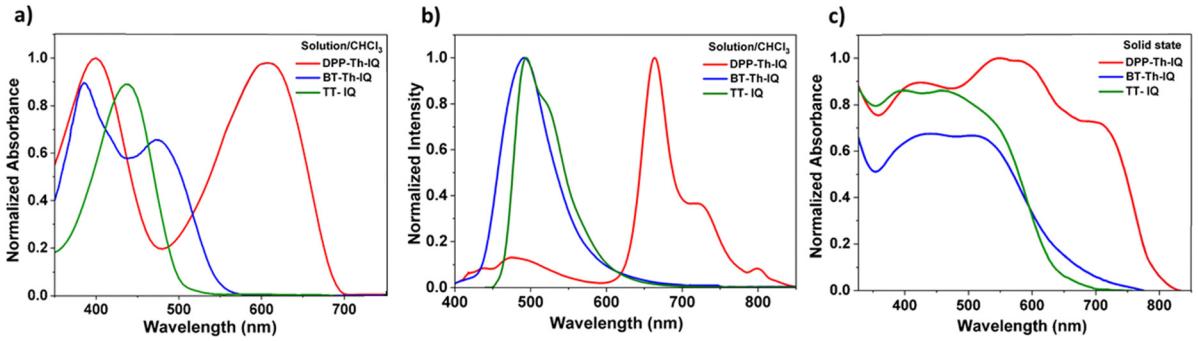

Fig. 3 (a) Normalized absorption (b) normalized emission spectra upon optical excitation at 390 nm, 415 nm and 385 nm for **DPP-Th-IQ**, **BT-Th-IQ** and **TT-IQ** respectively in chloroform (2.5 μg mL^{-1}) solution (c) thin-films absorption spectra profile of the synthesized SMDs.

peak value at 435 nm, **BT-Th-IQ** displayed absorption peaks at 386 nm and 480 nm.

DPP-Th-IQ exhibited the most red-shifted absorption maxima (λ_{max}^{abs}) in solution at 630 nm with an additional peak at 400 nm. The 630 nm peak reflects significant ICT attributed to its DPP core and extended conjugation through bridging thiophenes. By contrast, λ_{max}^{abs} in thin-film revealed a notable red shift to 710 nm, indicative of altered intermolecular interactions or π–π stacking in the solid state as shown in Fig. 3c. Whereas **BT-Th-IQ** SMD showed a most pronounced gap between its solution λ_{max}^{abs} 386 nm and thin-film λ_{max}^{abs} at 515 nm, underscoring the strongest influence of molecular packing on these materials.

The PL spectra of the SMDs were measured in dilute chloroform solutions and given in Fig. 3b. **DPP-Th-IQ** exhibited the most red-shifted emissions maxima λ_{max}^{emi} at 664 nm due to enhanced ICT.[46] Whereas, **BT-Th-IQ** and **TT-IQ** showed consistent emission maxima at 493 nm and 495 nm respectively. In Table 2 we further show the respective Stokes shifts (λ_{st}) for the SMDs calculated based on λ_{max}^{abs} and λ_{max}^{emi} differences. A relatively small λ_{st} of 34 nm in **DPP-Th-IQ** suggests minimal structural rearrangement in the excited state which is indicative that the chromophore can reduce the non-radiative energy losses and favor higher photocurrent generation.[47–50] Whereas, the large λ_{st} of 107 nm suggests a substantial reorganization of the **BT-Th-IQ** framework upon photoexcitation, which may offer avenues for exciton management. Meanwhile, **TT-IQ** SMD, featuring a TT core having λ_{max}^{abs} at 435 nm and λ_{max}^{emi} at 495 nm in chloroform with respective λ_{st} of 60 nm has a lower spectral coverage, suggesting that strategic combination with complementary acceptors could exploit **TT-IQ**'s slightly higher energy gap to maximize overall solar absorption. The photoexcitation-states based charge transfer is further discussed in the subsequent sections.

Solvatochromic effect was investigated by recording UV-vis absorption and photoluminescence spectra in chlorobenzene, tetrahydrofuran, toluene, and methanol. The spectra are given in SI, Fig. S11 and detailed in Tables S2–S4. Among the synthesized SMDs, **DPP-Th-IQ** displayed the largest bathochromic response, with λ_{max}^{abs} shifting from 598–610 nm in non-polar media to 660 nm in methanol and λ_{max}^{emi} red-shifting from 660–665 nm to 800 nm with $\lambda_{st} \approx 140$ nm. The pronounced shift highlights strong ICT stabilization in polar environments.[51,52] **BT-Th-IQ** showed smaller absorption changes, such as from 380–387 nm to ~513 nm in methanol. Yet a sizable PL red-shift, which resulted in λ_{st} in the range 92–133 nm, indicated the polarity-induced excited-state reorganization. Whereas, **TT-IQ** SMD exhibited minimal solvent-dependent shifts in λ_{max}^{abs} (425–430 nm), yet its λ_{max}^{emi} exhibited considerable sensitivity, shifting from 485–490 nm in nonpolar solvents to 550 nm in methanol. This resulted in a significant increase in λ_{st} from about 57–65 nm in lower polarity solvents to up to 121 nm in highly polar methanol. The combined trends confirm that solvent polarity predominantly tunes excited-state relaxation,

Table 2 Optical characteristics of the synthesized **DPP-Th-IQ**, **BT-Th-IQ**, and **TT-IQ** SMDs

	Experimental				Theoretical				
Molecule	$\lambda_{sol.}^{abs}$ [a] (nm)	$\lambda_{fil.}^{abs}$ [a] (nm)	$\lambda_{sol.}^{emi}$ [a] (nm)	λ_{st} [b] (nm)	$\lambda_{theo.}^{abs}$ [c] (nm)	E_X [d] (eV)	μ_{tr} [d] (a.u.)	f [d]	C.I. [e]
DPP-Th-IQ	630	710	664	34	543	2.27	28.1	1.57	H → L (+68%) H → L+2 (+11%)
BT-Th-IQ	386	515	493	107	503	2.46	31.5	1.87	H → L (+67%) H−4 → L (+10%)
TT-IQ	435	460	495	60	388	3.19	38.5	2.85	H → L (+63%) H−3 → L+1 (+20%)

[a] Wavelengths of the absorption/emission maxima ($\lambda_{sol.}^{abs}/\lambda_{sol.}^{emi}$) in chloroform solutions (2.5 μg mL^{-1}) and in film ($\lambda_{fil.}^{emi}$) at wavelengths of 410 nm. [b] Stokes shift (λ_{st}) calculated from absorption and emission maxima difference. [c] Theoretically calculated absorption maxima ($\lambda_{theo.}^{abs}$). [d] S_0–S_1 state excitation energy (E_X), transition electric dipole moment (μ_{tr}), and oscillatory strength (f). [e] Orbitals charge transfer configuration interactions (C.I.), simulated by TD-DFT/CAM-B3LYP/6-31G(d,p) method.

with **DPP-Th-IQ** experiencing the greatest ICT-driven stabilization.

Additionally, the TD-DFT simulations with CAM-B3LYP/6-31G(d,p) method were carried out and given in Table 2. Computational results support the experimental findings by predicting λ_{theo}^{abs} values that mirror the observed red-blue absorption trends. Specifically, **DPP-Th-IQ** and **BT-Th-IQ** reveal relatively low-energy electronic transitions at 543 nm and 503 nm, respectively, while **TT-IQ** appears more blue-shifted at 388 nm. The S_0–S_1 excitation energy (E_X), transition dipole moment (μ_{tr}), and oscillator strength (f) offer additional insights into each SMD's propensity for strong light absorption and effective exciton generation which is a critical parameter for high photocurrent in OSC. Notably, **TT-IQ** exhibits the largest μ_{tr} (38.5 a.u.) and highest f (2.85), underscoring a particularly intense transition. Molecular orbitals configuration interaction (C.I.) analyses further confirmed that these prominent absorptions arise primarily from the HOMO → LUMO transitions, supplemented by minor contributions from nearby orbitals such as HOMO → LUMO+2 in **DPP-Th-IQ** and HOMO−4 → LUMO in **BT-Th-IQ**. Overall, these photophysical characteristics highlight the importance of structural tuning in SMDs. **DPP-Th-IQ** leverages a strongly red-shifted profile that can capture lower-energy photons, **BT-Th-IQ** gains considerable absorption enhancement in the solid state, and **TT-IQ** offers robust transition strengths and moderate film-phase shifts.

Based on the above experimental and computational optoelectronic analysis, the synthesized SMDs showcase varied trends in molecular interactions, processing conditions, and CT behavior. For instance, the **DPP-Th-IQ** SMD, with its highly sensitive ICT response and red-shifted absorption, suggests strong D/A interactions in BHJ blends. Its ability to maintain broad absorption in various solvent environments makes it an excellent candidate for low-bandgap OSCs. **BT-Th-IQ**, showing high film-phase aggregation and moderate solvatochromic effects, suggests potential as a highly tunable donor, where solvent engineering can be leveraged to optimize film morphology and charge mobility. **TT-IQ**, with high oscillator strength and moderate solvatochromic shifts, could serve as a complementary donor in multi-component blends, where its higher transition dipole moment may enhance CT at D/A interfaces.

3.5. Thermal and photostability

The photostability of the IQ-based SMDs was assessed in the thin-film state. Thin films were prepared by spin-coating (0.1 mg mL^{-1}) chlorobenzene solutions onto pre-cleaned quartz substrates (1 × 1 cm^2) at 2000 rpm for 60 s, followed by thermal annealing at 100 °C for 20 minutes under vacuum to remove residual solvent and enhance molecular ordering. The films were then exposed to continuous AM 1.5G solar irradiation (100 mW cm^{-2}) for 30 h under ambient conditions. Photo degradation was monitored by UV-vis absorption spectroscopy at regular intervals. The evolution of normalized absorbance over time is presented in SI, Fig. S13a–c, with comparative stability data summarized in Table S5. All SMDs demonstrated excellent photo stability up to 90% retained absorbance after exposure for 30 hours.

To investigate thermal behavior and molecular interactions, temperature-dependent UV-vis absorption measurements were conducted in chlorobenzene (0.1 mg mL^{-1}) over the range of 20 °C to 120 °C. Spectra are shown in SI, Fig. S13d–f. **DPP-Th-IQ** and **BT-Th-IQ** showed minimal bathochromic shifts and modest intensity changes with temperature which indicates stable π–π interactions/aggregation states that persist upon heating. In contrast, **TT-IQ** displayed more noticeable intensity variations at elevated temperature, pointing to comparatively weaker intermolecular interactions. Thermal stability was further evaluated by TGA under nitrogen atmosphere at a heating rate of 10 °C min^{-1}. As shown in the TGA profiles in SI, Fig. S14, the 5% mass-loss temperatures (T_5%) exceeded 250 °C for all SMDs and were highest for **BT-Th-IQ** ∼410 °C and **DPP-Th-IQ** ∼400 °C, with **TT-IQ** the lowest ∼270 °C. The high decomposition thresholds of **DPP-Th-IQ** and **BT-Th-IQ** define comfortable processing windows and support their robustness during solution deposition and post-deposition annealing.

3.6. Reorganization energy and solvation free energy

Charge transport in OSCs is governed by the ability of the donor and acceptor molecules to efficiently facilitate charge hopping. This efficiency is quantified by the reorganization energy, which represents the energy associated with structural relaxation upon CT.[53,54] Herein, λ_{hole} and λ_{ele} were calculated for the SMDs and the **Y6** NFA *via* B3LYP/6-31G(d,p) method to determine hole and electron mobility, respectively. The results are summarized in Table 3.

Among the SMDs, **BT-Th-IQ** exhibited the lowest λ_{hole} (0.255 eV), followed closely by **TT-IQ** (0.258 eV), and **DPP-Th-IQ** (0.288 eV). The relatively low λ_{hole} of **BT-Th-IQ** suggests that it possesses the most favorable hole transport properties among the three donors, as a lower hole reorganization energy reduces charge-trapping losses and enhances carrier mobility. The BT core likely contributes to this reduced reorganization energy by minimizing geometric relaxation upon oxidation, leading to more efficient hole transport. In contrast, **DPP-Th-IQ** exhibited the highest λ_{hole} (0.288 eV), suggesting that it experiences greater structural distortion upon hole injection, potentially due to localized charge distribution in the oxidized state. For electron transport, **DPP-Th-IQ** exhibited the lowest λ_{elec} (0.213 eV), which is favorable for robust electron transport

Table 3 Hole/electron reorganization energy ($\lambda_{hole}/\lambda_{ele}$) calculated by B3LYP/6-31G(d,p) method and dipole moment in ground-state (μ_g) and excited-state (μ_e) with respective Gibbs solvation-free energy (ΔG_{solv}) in chloroform solvent calculated using M06-2X/6-31G(d,p) method *via* SMD solvation model

Molecule	λ_{hole} (eV)	λ_{ele} (eV)	μ_g (Debye)	μ_e (Debye)	$\Delta\mu$ (Debye)	ΔG_{solv} (kcal mol^{-1})
DPP-Th-IQ	0.288	0.213	2.55	3.22	0.67	−40.84
BT-Th-IQ	0.255	0.237	3.43	4.47	1.04	−37.94
TT-IQ	0.258	0.241	2.44	3.09	0.67	−31.92
Y6	0.160	0.150	1.07	1.89	0.82	−14.61

Table 4 Electron transition density properties of the designed SMDs including charge transfer distance (D_{CT}), H_{index}, t_{index}, intrinsic charge transfer (CT) excitation, intrinsic local excitation (LE), transferred charge (q_{CT}), hole/electron delocalization index (HDI/EDI), and exciton binding energy (E_B) simulated by TD-DFT/CAM-B3LYP method

Molecule	D_{CT} (Å)	H_{index} (Å)	t_{index} (Å)	CT (%)	q_{CT} (e^-)	LE (%)	HDI	EDI	E_B (eV)
DPP-Th-IQ	0.06	4.59	−0.88	57.75	0.38	42.25	5.78	5.68	0.41
BT-Th-IQ	0.87	4.84	−0.98	65.22	0.48	34.77	5.00	5.70	0.31
TT-IQ	0.11	6.18	−0.76	48.95	0.43	51.05	4.83	4.20	0.44

due to the electron-deficient nature of the DPP core, which stabilizes the negative charge upon reduction and reduces the structural reorganization for CT. On the other hand, **BT-Th-IQ** and **TT-IQ** have slightly higher λ_{ele} (0.237 eV and 0.241 eV, respectively), indicating marginally less electron transport efficiency than **DPP-Th-IQ**. Moreover, for efficient charge separation and transport in photoactive layer, the reorganization energies of donors and acceptors should be well balanced.[55,56] The benchmark NFA **Y6** exhibits significantly lower λ_{hole} (0.160 eV) and λ_{ele} (0.150 eV), reinforcing its role as an efficient charge transporter. The lower reorganization energy of **Y6** confirms that it can readily accept electrons from SMDs, minimizing energy loss during charge separation and facilitating long-lived charge carriers in photoactive layer. Comparatively the SMDs have higher λ_{hole} values than **Y6**, suggesting that hole transport is slightly less efficient than electron transport. However, the relatively small gap between λ_{hole} and λ_{ele} in the three SMDs suggests that these molecules can still achieve balanced charge transport, an important factor in reducing charge recombination and increasing FF in OSCs. These results show that the IQ-capped molecules are excellent candidates for high-performance OSCs, particularly when paired with low-reorganization-energy acceptors like **Y6**.

Additionally, the molecular polarity, charge redistribution, and solubility are the other key parameters which are influenced by the dipole moment and solvation free energy and greatly affect film morphology and charge transport in OSCs.[43,57] Herein, the dipole moment and Gibbs solvation-free energy (ΔG_{solv}) were further computed *via* M06-2X/6-31G(d,p) method in chloroform solvent. Results given in Table 3 show that among SMDs, **BT-Th-IQ** exhibited the highest ground-state dipole moment (μ_g = 3.43 D) and excited-state dipole moment (μ_e = 4.47 D), with the largest dipole moment variation ($\Delta\mu$ = 1.04 D). This indicates strong charge redistribution upon excitation, consistent with its high CT character. **DPP-Th-IQ** and **TT-IQ** exhibited lower dipole moment variation ($\Delta\mu$ = 0.67 D), suggesting moderate ICT contributions, while **Y6** displays a dipole moment variation ($\Delta\mu$ = 0.82 D), indicating a moderate degree of charge separation. Whereas, **DPP-Th-IQ** exhibited the most negative ΔG_{solv} (−40.84 kcal mol^{-1}), followed by **BT-Th-IQ** (−37.94 kcal mol^{-1}) and **TT-IQ** (−31.92 kcal mol^{-1}), indicating that **DPP-Th-IQ** has the highest solubility in chloroform, which may aid in better thin-film formation.

3.7. Intramolecular charge transfer and transition density analysis

ICT and exciton dissociation play a pivotal role in the performance of the OSCs.[54] To comprehend the photoexcitation dynamics of the synthesized SMDs, a detailed electron transition density analysis was performed based on TD-DFT/CAM-B3LYP/6-31G(d,p) calculations in MultiWfn 3.8. The analysis includes key electron transition properties such as CT distance (D_{CT}), H_{index}, t_{index}, intrinsic CT excitation, intrinsic local excitation (LE), transferred charge (q_{CT}), hole/electron delocalization indices (HDI/EDI), and exciton binding energy (E_B), as summarized in Table 4.[21,29] To visualize the charge distribution, electron density difference (EDD) contours, hole/electron heat maps, and transition density matrix (TDM) heat maps were also generated and given in Fig. 4.

As shown in the EDD graphs showcasing holes (cyan) and electrons (blue) delocalization in Fig. 4a and respective heat maps in Fig. 4b, the holes (59.1%) and electrons (50.8%) are predominantly localized on the DPP core, with moderate contributions from the thiophene bridges (29.5% for holes, 36.5% for electrons) and minimal distribution in the side IQ units (11.4% for holes, 12.6% for electrons) in **DPP-Th-IQ** SMD. This suggests strong electronic coupling between the DPP core and thiophene bridges, which enhances charge delocalization. In **BT-Th-IQ**, electrons are mostly concentrated on the BT core (66.2%), whereas holes are mainly distributed over the thiophene bridges (51.4%), indicating a well-defined charge-separated state that facilitates charge extraction. In **TT-IQ**, holes (46.7%) and electrons (34.1%) are more evenly distributed across the molecular skeleton, particularly between the TT core and IQ end-groups. This widespread delocalization enhances charge transport but may also increase hole/electron recombination. TDM heat maps in Fig. 4c further illustrate the extent of hole/electron spatial overlap within different molecular segments. Regular hole and electron generation patterns observed across all three SMDs indicate efficient charge separation, particularly in **BT-Th-IQ** and **DPP-Th-IQ**. These findings suggest that all three donors exhibited well-defined ICT characteristics, which are favorable for charge transport and exciton dissociation in OSCs.

D_{CT} provides a measure of the spatial charge separation in the excited state, influencing exciton dissociation efficiency. Among the three SMDs, **BT-Th-IQ** exhibited the largest D_{CT} (0.87 Å), followed by **TT-IQ** (0.11 Å) and **DPP-Th-IQ** (0.06 Å), indicating that **BT-Th-IQ** exhibits the most significant charge separation upon photoexcitation. A higher D_{CT} value suggests stronger charge separation, which is beneficial for reducing recombination and promoting efficient charge extraction in OSCs. Conversely, **DPP-Th-IQ** shows a lower D_{CT}, suggesting a more localized excitonic state. CT and LE components further characterize the nature of the electronic transitions. **BT-Th-IQ** exhibits the highest CT contribution (65.2%), indicating a

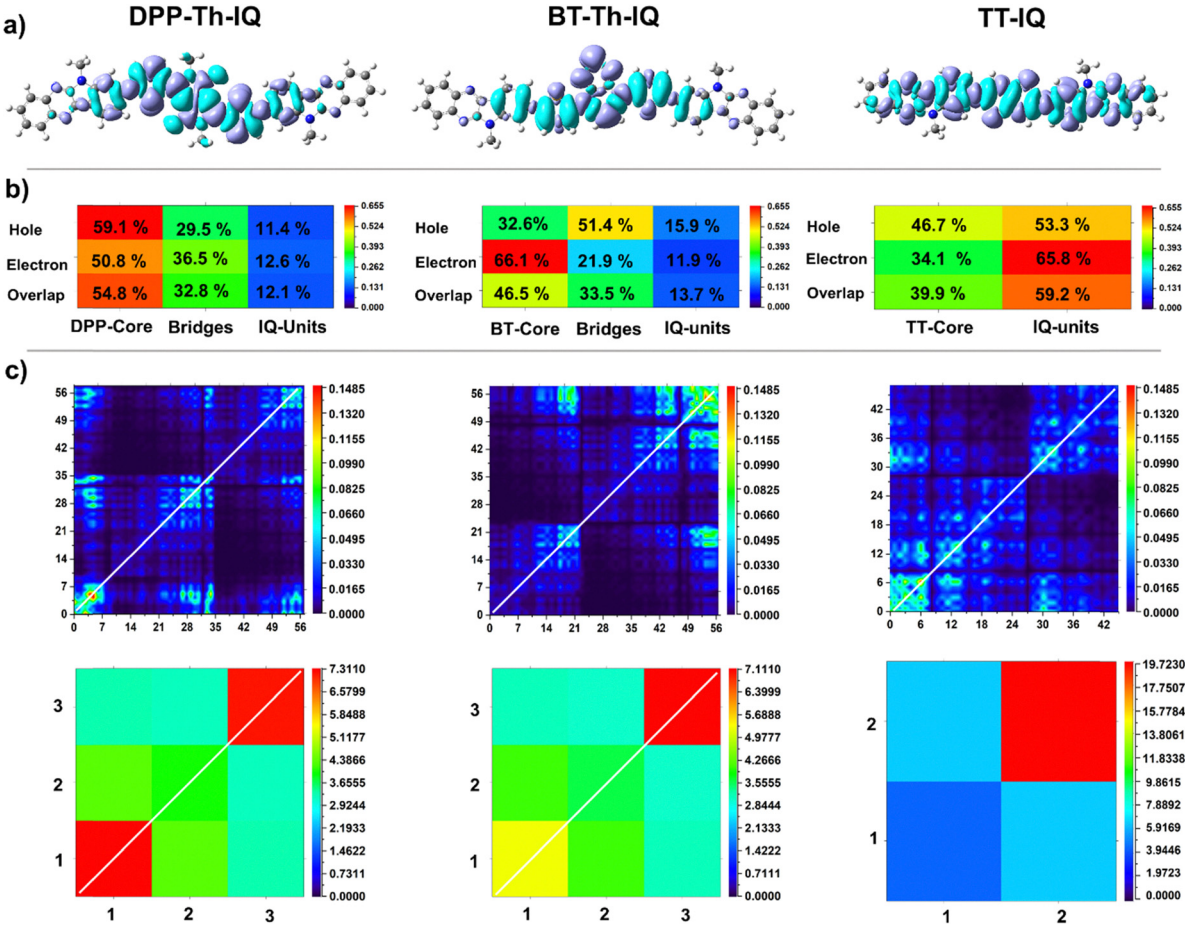

Fig. 4 (a) Electron density difference (EDD) surface contours, (b) hole/electron heat maps with percentage delocalization and spatial overlap within core units, thiophene bridges, and end-group IQs, (c) and transition density matrix (TDM) heat maps for atoms and molecular fragments such as core units (1), thiophene bridges (2), and side IQs units (3), simulated *via* TD-DFT/CAM-B3LYP method.

highly polarized charge distribution that favors efficient charge transfer. In comparison, **DPP-Th-IQ** (57.7%) and **TT-IQ** (48.9%) exhibit lower CT contributions, with **TT-IQ** displaying the highest LE component (51.1%), suggesting a more localized charge distribution. These findings confirm that **BT-Th-IQ** is the most promising donor for achieving long-range charge separation, while **TT-IQ**, with its higher LE component, may rely more on intermolecular interactions to facilitate charge transport.

The parameter q_{CT} further provides quantitative measure of charge redistribution in the excited state. From the results, **BT-Th-IQ** exhibited the highest q_{CT} ($0.48e^-$), followed by **TT-IQ** ($0.43e^-$) and **DPP-Th-IQ** ($0.38e^-$). The larger q_{CT} of **BT-Th-IQ** confirms strong ICT behavior, which is beneficial for reducing energy loss during charge transport. HDI and EDI further indicate the extent of charge delocalization across the molecular framework. **DPP-Th-IQ** SMD having HDI/EDI of 5.78/5.68 and **BT-Th-IQ** with HDI/EDI 5.00/5.70 exhibited widespread charge delocalization, facilitating charge hopping and improving charge mobility. Whereas, **TT-IQ**, with lower HDI/EDI of 4.83/4.20, suggests a more localized charge transport pathway. Furthermore, the **BT-Th-IQ** SMD exhibited the lowest E_B (0.31 eV), followed by **DPP-Th-IQ** (0.41 eV) and **TT-IQ** (0.44 eV). The reduced E_B in **BT-Th-IQ** is attributed to its high CT character and significant charge transfer distance, further reinforcing its higher charge transport characteristics. The slightly higher E_B in **TT-IQ** suggests a more tightly bound excitonic state, which may require an optimized D/A interface to enhance charge dissociation.

3.8. Donor/acceptor interfacial charge transfer properties

Efficient interfacial CT at the D/A interface plays a pivotal role in determining the performance of OSCs, as it critically affects CT state dissociation and free-charge generation.[58] To explore CT characteristics, the interfacial packing, excited-state configurations, and CT mechanisms of complexes formed between the synthesized SMDs and the benchmark **Y6** NFA were studied. Initially, optimized face-on orientation configurations of D/A complexes were constructed with an initial donor–acceptor separation of 3.5 Å. Geometry optimization was carried out at the B3LYP/6-31G(d,p) level, followed by TD-DFT calculations with the RSH functional CAM-B3LYP and the CT analysis based on EDD method *via* MultiWfn 3.8.[59,60]

The optimized D/A complex geometries given in Fig. 5a and b, demonstrated distinct intermolecular arrangements for each

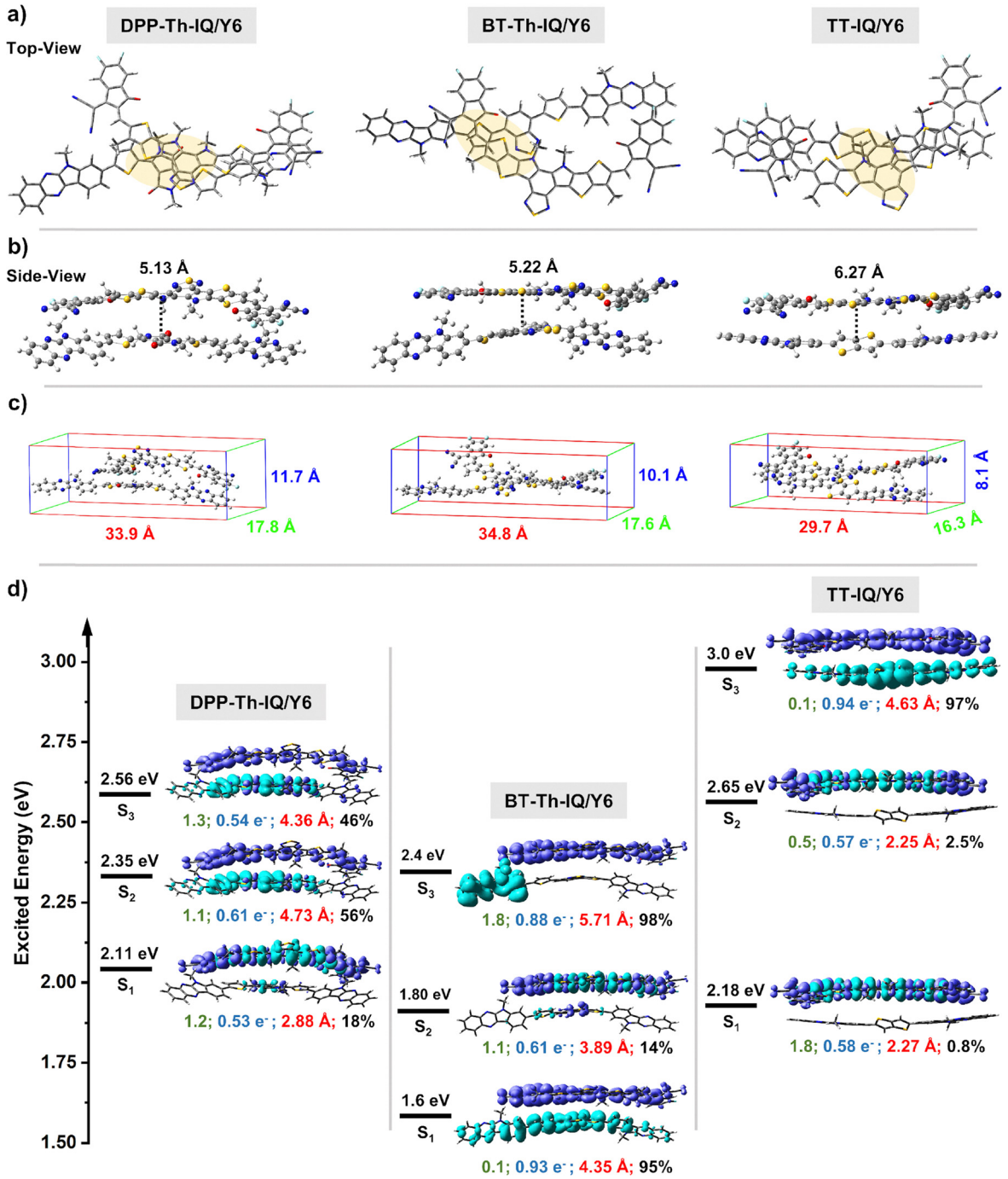

Fig. 5 (a) and (b) Top and side views of the optimized face-on D/A complexes (**DPP-Th-IQ/Y6**, **BT-Th-IQ/Y6**, and **TT-IQ/Y6**) obtained at the DFT/B3LYP/6-31G(d,p) level, illustrating the π–π stacking orientation and centroid-to-centroid distances. (c) Dimensional analysis of length, width, and height of each simulated D/A complex. (d) Low-lying excited-state properties (S_1–S_3) derived from TD-DFT/CAM-B3LYP/6-31G(d,p) calculations based on EDD method, highlighting excitation energies, oscillator strengths (green), transferred charge (blue), charge transfer distance index (red), and CT excitation percentages (black) for each donor/**Y6** complex and their respective EDD isosurfaces.

donor when combined with **Y6**. All three complexes **DPP-Th-IQ/Y6**, **BT-Th-IQ/Y6**, and **TT-IQ/Y6** exhibited a preferred face-on π–π stacking orientation, facilitating strong intermolecular electronic interactions. Notably, the **TT-IQ/Y6** complex displayed the largest intermolecular π–π stacking area, indicative of extensive D/A interfacial overlap. However, despite the smaller stacking areas, the **DPP-Th-IQ/Y6** and **BT-Th-IQ/Y6** complexes exhibit significantly shorter centroid-to-centroid distances of 5.13 Å and 5.22 Å, respectively, compared to **TT-IQ/Y6** at 6.27 Å. These shorter distances imply stronger intermolecular interactions and closer packing arrangements driven by the favorable electronic coupling of the DPP and BT cores

with **Y6**. Further structural dimensions were measured to analyze the molecular packing in D/A complexes. As shown in Fig. 5c, the lengths of the **DPP-Th-IQ/Y6**, **BT-Th-IQ/Y6**, and **TT-IQ/Y6** complexes are 33.9 Å, 34.8 Å, and 29.7 Å, respectively, with widths of 17.8 Å, 17.6 Å, and 16.3 Å, and heights of 11.7 Å, 10.1 Å, and 8.1 Å, respectively. Side-view packing configurations and dimensional data revealed well-defined and stable intermolecular stacking patterns as characterized by parallel alignment and slightly curved ''half-bowl'' conformations.

Excited-state vertical transitions and interfacial CT behaviors for the lowest three excited states (S_1–S_3) were thoroughly evaluated for the D/A complexes and described in Fig. 5d. The EDD method allows clear visualization of electron transition processes as ''hole → electron'' distributions, categorizing excited states into Frenkel excitons (localized) and pure/hybrid CT states (electron and hole spatially separated across donor and acceptor). For the **DPP-Th-IQ/Y6** complex, the lowest-energy excited state (S_1 at 2.11 eV, f = 1.2) shows moderate charge transfer (CT ≈ 18%, q_{CT} = 0.53e$^-$, D_{index} = 2.88 Å), predominantly acceptor-localized with ≈90% hole/electron localization on **Y6**. However, higher-energy states such as S_2 (2.35 eV, 56% CT, 4.73 Å D_{index}) and S_3 (2.56 eV, 46% CT, 4.36 Å D_{index}) exhibit increased charge separation, suggesting an enhanced likelihood of exciton dissociation at elevated excitation energies. EDD contours confirm this, demonstrating progressively stronger donor-involved CT contributions at these higher states. In contrast, the S_1 excitation in **TT-IQ/Y6** at 2.18 and subsequent excited state S_2 at 2.60 eV shows minimal charge separation (0–2.5% CT), indicating the presence of localized Frenkel-type excitations at lowest and intermediate states. However, the third excited state S_3 at 3.0 eV recovers robust CT characteristics (97% CT, q_{CT} = 0.94e$^-$, D_{index} = 4.63 Å). These findings confirm that **TT-IQ/Y6** also presents suitable excited-state charge-transfer dynamics conducive to efficient exciton dissociation.

Overall, the interfacial mechanistic analysis suggests that among the modelled SMDs/**Y6** complexes, **BT-Th-IQ/Y6** exhibits the high CT percentages, substantial transferred charges, and significant spatial electron–hole separation distances, all beneficial for promoting efficient CT state dissociation and charge generation. **DPP-Th-IQ/Y6**, despite its smaller π–π stacking distance, efficiently achieves notable CT character and robust excited-state interactions. Whereas, the **TT-IQ/Y6** complex, with broader π–π stacking and moderate interfacial CT distances, also demonstrates effective charge separation dynamics. Thus, all three donor complexes demonstrate favorable excited-state and structural characteristics at the molecular interface with the **Y6** acceptor, highlighting their potential in the design and fabrication of future ASM-OSCs.

4. Conclusions

In this work, three SMDs named **DPP-Th-IQ**, **BT-Th-IQ**, and **TT-IQ**, were successfully designed, synthesized, and characterized for potential application in next-generation ASM-OSCs. Incorporating easily synthesized IQ-terminal moieties, combined with electron-deficient diketopyrrolopyrrole and benzothiadiazole cores, as well as an electron-rich thienothiophene core, we systematically explored the impact of structural motifs on their electronic, optical, charge transport, interfacial charge transfer properties and molecular stability. The strategically designed SMDs featuring a streamlined cost-efficient synthesis is beneficial for scalability, paving the way for potential commercial applications in future ASM-OSCs.

Electrochemical and DFT calculations revealed well-matched HOMO–LUMO offsets with the **Y6** acceptor, indicating sufficient driving force for exciton dissociation into free charges. Notably, **DPP-Th-IQ** exhibited significantly improved optical properties, including redshift in λ_{max}^{abs} (630 nm) and λ_{emi}^{abs} (664 nm), the smallest electrochemical bandgap (1.65 eV), offering extended absorption in the visible–near-infrared range, in addition to improved solvation properties (ΔG_{solv} = −40.84 kcal mol^{-1}), which can facilitate solution-processing and film formation. Moreover, the lowest electron reorganization energy (0.213 eV) of **DPP-Th-IQ**, highlighting its capacity for swift electron transfer. Meanwhile, **BT-Th-IQ** demonstrated the highest charge transfer character (CT = 65.22%) and the longest charge transfer distance (D_{CT} = 0.87 Å), accompanied with the lowest exciton binding energy (0.31 eV) and low hole reorganization energy (0.255 eV) for improved hole mobility positioning it as the most promising donor for long-range charge separation. Moreover **BT-Th-IQ** showed a notable red shift in thin film (386–515 nm) reflecting film-phase interactions to effective charge transport, while **TT-IQ** exhibited balanced hole/electron delocalization, making it a useful complementary donor in OSC architectures. Whereas, the interfacial analysis of optimized donor/**Y6** complexes demonstrated stable face-on π–π stacking configurations with robust D/A interactions. **BT-Th-IQ/Y6** complex yielded efficient CT states, underpinning their potential for high J_{SC}. **DPP-Th-IQ/Y6** complex showed enhanced interfacial CT indicating favorable structural attributes for achieving high charge transport mobilities. Although **TT-IQ/Y6** demonstrated extensive interfacial stacking, its variable CT efficiency across excitation energies highlighted the need for precise morphological optimization to ensure consistent device performance. Importantly, the materials exhibited encouraging durability. Thin films retained ≥90% of their initial absorbance after 30 h of continuous AM 1.5G irradiation (100 mW cm^{-2}), evidencing good photostability under operationally relevant conditions. Thermogravimetric analysis indicates T_d, 5% > 250 °C for all donors, underscoring robust thermal stability.

Overall, our findings provide valuable molecular-design insights. Among the three donors, **BT-Th-IQ** showed the highest intrinsic charge-separation fraction, lowest exciton-binding energy, and the most balanced hole/electron reorganization energies, together with robust face-on π–π stacking with **Y6**. These traits favor efficient CT state dissociation and balanced carrier transport. **DPP-Th-IQ** and **TT-IQ** exhibited complementary strengths, such as deeper HOMO for higher V_{OC} and symmetric hole delocalization. The present work therefore

establishes a detailed atomistic structure–property framework that sets critical benchmarks for subsequent optimization. Full photovoltaic device fabrication and characterization (V_{OC}, J_{SC}, fill factor and PCE measurements) are proposed as the logical next step to realize the performance potential of these IQ-capped small-molecule donors in all-small-molecule OSC architectures.

Author contributions

Maryam Javed: synthesis, purification, experimental characterization, formal analysis, investigation, writing – original draft. Waqas Akram: synthesis, experimental characterization, computational methodology, formal analysis, data curation, visualization, investigation, writing – original draft. Zeeshan Ali: experimental methodology, synthesis, characterization. Nabeel Shahzad: software, computational analysis, data curation, visualization. Munazza Shahid: conceptualization, writing – review & editing. Ghayoor Abbas Chotana: resources, software, methodology. Jafar Iqbal Khan: methodology, validation, writing – review & editing. Jie Min: data curation, validation, resources. Muhammad Altaf: methodology, validation, data curation. Christian B. Nielsen: methodology, writing – review & editing. Raja Shahid Ashraf: conceptualization, supervision, resources, methodology, funding accusation, project administration.

Conflicts of interest

There are no conflicts to declare.

Data availability

The data supporting this article have been included as part of the SI. Supplementary information: Detailed experimental procedures for the synthesis of the new SMDs, including characterization data and simulation results supporting the findings in the main manuscript. See DOI: **https://doi.org/10.1039/d5tc02318a**.

Acknowledgements

We are grateful to the Higher Education Commission Pakistan's NRPU project (17546). We also acknowledge Office of Research and Innovation Commercialization (ORIC) Department, Government College University and Department of Chemistry and Chemical Engineering, Lahore University of Management Sciences for supporting this research.

References

1 S. K. Karunakaran, G. M. Arumugam, W. Yang, S. Ge, S. N. Khan, X. Lin and G. Yang, Recent progress in inkjet-printed solar cells, *J. Mater. Chem. A*, 2019, **7**(23), 13873–13902.
2 M. P. Tsang, G. W. Sonnemann and D. M. Bassani, Life-cycle assessment of cradle-to-grave opportunities and environmental impacts of organic photovoltaic solar panels compared to conventional technologies, *Sol. Energy Mater. Sol. Cells*, 2016, **156**, 37–48.
3 D. J. Lipomi, Organic photovoltaics: focus on its strengths, *Joule*, 2018, **2**(2), 195–198.
4 J. Zhao, Y. Li, G. Yang, K. Jiang, H. Lin, H. Ade, W. Ma and H. Yan, Efficient organic solar cells processed from hydrocarbon solvents, *Nat. Energy*, 2016, **1**(2), 1–7.
5 R. Ganesamoorthy, G. Sathiyan and P. Sakthivel, Fullerene based acceptors for efficient bulk heterojunction organic solar cell applications, *Sol. Energy Mater. Sol. Cells*, 2017, **161**, 102–148.
6 C. Li, J. Song, H. Lai, H. Zhang, R. Zhou, J. Xu, H. Huang, L. Liu, J. Gao and Y. Li, Non-fullerene acceptors with high crystallinity and photoluminescence quantum yield enable >20% efficiency organic solar cells, *Nat. Mater.*, 2025, 1–11.
7 Q. Liu, Y. Jiang, K. Jin, J. Qin, J. Xu, W. Li, J. Xiong, J. Liu, Z. Xiao and K. Sun, 18% Efficiency organic solar cells, *Sci. Bull.*, 2020, **65**(4), 272–275.
8 B. Kan, Y. Kan, L. Zuo, X. Shi and K. Gao, Recent progress on all-small molecule organic solar cells using small-molecule nonfullerene acceptors, *InfoMat*, 2021, **3**(2), 175–200.
9 H. Gao, Y. Sun, L. Meng, C. Han, X. Wan and Y. Chen, Recent progress in all-small-molecule organic solar cells, *Small*, 2023, **19**(3), 2205594.
10 Y. Liu, X. Wan, F. Wang, J. Zhou, G. Long, J. Tian and Y. Chen, High-performance solar cells using a solution-processed small molecule containing benzodithiophene unit, *Adv. Mater.*, 2011, **23**(45), 5387–5391.
11 J. Zhou, X. Wan, Y. Liu, Y. Zuo, Z. Li, G. He, G. Long, W. Ni, C. Li, X. Su and Y. Chen, Small molecules based on benzo[1,2-*b*:4,5-*b*′]dithiophene unit for high-performance solution-processed organic solar cells, *J. Am. Chem. Soc.*, 2012, **134**(39), 16345–16351.
12 J. Ge, L. Hong, W. Song, L. Xie, J. Zhang, Z. Chen, K. Yu, R. Peng, X. Zhang and Z. Ge, Solvent annealing enables 15.39% efficiency all-small-molecule solar cells through improved molecule interconnection and reduced non-radiative loss, *Adv. Energy Mater.*, 2021, **11**(22), 2100800.
13 T. Shan, K. Ding, L. Yu, X. Wang, Y. Zhang, X. Zheng, C. C. Chen, Q. Peng and H. Zhong, Spatially orthogonal 2D sidechains optimize morphology in all-small-molecule organic solar cells, *Adv. Funct. Mater.*, 2021, **31**(24), 2100750.
14 L. Xiao, C. Yan, Z. Li, W. Zhong, W. Tan, Y. Liu, F. Liu, X. Peng and Y. Min, Morphology evolution induced by sequential annealing enabling enhanced efficiency in all-small molecule solar cells, *ACS Appl. Energy Mater.*, 2021, **4**(4), 4234–4241.
15 R. Sun, Y. Wu, J. Guo, Z. Luo, C. Yang and J. Min, High-efficiency all-small-molecule organic solar cells based on an organic molecule donor with an asymmetric thieno[2,3-*f*]benzofuran unit, *Sci. China Chem.*, 2020, **63**, 1246–1255.
16 D. Hu, H. Tang, S. Karuthedath, Q. Chen, S. Chen, J. I. Khan, H. Liu, Q. Yang, J. Gorenflot and C. E. Petoukhoff, A volatile

solid additive enables oligothiophene all-small-molecule organic solar cells with excellent commercial viability, *Adv. Funct. Mater.*, 2023, **33**(6), 2211873.
17 J. Yi, G. Zhang, H. Yu and H. Yan, Advantages, challenges and molecular design of different material types used in organic solar cells, *Nat. Rev. Mater.*, 2024, **9**(1), 46–62.
18 M. C. Scharber, D. Mühlbacher, M. Koppe, P. Denk, C. Waldauf, A. J. Heeger and C. J. Brabec, Design rules for donors in bulk-heterojunction solar cells—Towards 10% energy-conversion efficiency, *Adv. Mater.*, 2006, **18**(6), 789–794.
19 N. K. Elumalai and A. Uddin, Open circuit voltage of organic solar cells: an in-depth review, *Energy Environ. Sci.*, 2016, **9**(2), 391–410.
20 C. Poelking, M. Tietze, C. Elschner, S. Olthof, D. Hertel, B. Baumeier, F. Würthner, K. Meerholz, K. Leo and D. Andrienko, Impact of mesoscale order on open-circuit voltage in organic solar cells, *Nat. Mater.*, 2015, **14**(4), 434–439.
21 T. Le Bahers, C. Adamo and I. Ciofini, A qualitative index of spatial extent in charge-transfer excitations, *J. Chem. Theory Comput.*, 2011, **7**(8), 2498–2506.
22 W. Kohn and L. J. Sham, Self-consistent equations including exchange and correlation effects, *Phys. Rev.*, 1965, **140**(4A), A1133.
23 M. J. Frisch, G. W. Trucks, H. B. Schlegel, G. E. Scuseria, M. A. Robb, J. R. Cheeseman, G. Scalmani, V. Barone, B. Mennucci and G. A. Petersson, *Gaussian 09, Revision D.01*, Gaussian, Inc., Wallingford CT, 2009, see also: URL: **https://www.gaussian.com**.
24 M. E. Casida, Time-dependent density functional response theory for molecules, *Recent Advances In Density Functional Methods: (Part I)*, World Scientific, 1995, pp. 155–192.
25 A. D. Becke, Density-functional thermochemistry. I. The effect of the exchange-only gradient correction, *J. Chem. Phys.*, 1992, **96**(3), 2155–2160.
26 J. W. Ochterski, G. A. Petersson and J. A. Montgomery Jr, A complete basis set model chemistry. V. Extensions to six or more heavy atoms, *J. Chem. Phys.*, 1996, **104**(7), 2598–2619.
27 A. Tenderholt, *PyMOlyze, Version 1.1*, Stanford University, Stanford, 2006, vol. 4, pp. 580–592.
28 J. Tomasi, B. Mennucci and E. Cancès, The IEF version of the PCM solvation method: an overview of a new method addressed to study molecular solutes at the QM ab initio level, *THEOCHEM*, 1999, **464**(1–3), 211–226.
29 X. Liu, S. Ma, Y. Ding, J. Gao, X. Liu, J. Yao and S. Dai, Molecular engineering of simple carbazole-triphenylamine hole transporting materials by replacing benzene with pyridine unit for perovskite solar cells, *Solar RRL*, 2019, **3**(5), 1800337.
30 D. Mester and M. Kállay, Charge-transfer excitations within density functional theory: How accurate are the most recommended approaches?, *J. Chem. Theory Comput.*, 2022, **18**(3), 1646–1662.
31 C. A. Guido, P. Cortona, B. Mennucci and C. Adamo, On the metric of charge transfer molecular excitations: a simple chemical descriptor, *J. Chem. Theory Comput.*, 2013, **9**(7), 3118–3126.
32 F. Coppola, P. Cimino, U. Raucci, M. G. Chiariello, A. Petrone and N. Rega, Exploring the Franck–Condon region of a photoexcited charge transfer complex in solution to interpret femtosecond stimulated Raman spectroscopy: Excited state electronic structure methods to unveil non-radiative pathways, *Chem. Sci.*, 2021, **12**(23), 8058–8072.
33 F. Coppola, P. Cimino, A. Petrone and N. Rega, Evidence of excited-state vibrational mode governing the photorelaxation of a charge-transfer complex, *J. Phys. Chem. A*, 2024, **128**(9), 1620–1633.
34 G. Sini, J. S. Sears and J.-L. Brédas, Evaluating the performance of DFT functionals in assessing the interaction energy and ground-state charge transfer of donor/acceptor complexes: tetrathiafulvalene− tetracyanoquinodimethane (TTF− TCNQ) as a model case, *J. Chem. Theory Comput.*, 2011, **7**(3), 602–609.
35 T. Lu and F. Chen, Multiwfn: a multifunctional wavefunction analyzer, *J. Comput. Chem.*, 2012, **33**(5), 580–592.
36 G. R. Hutchison, M. A. Ratner and T. J. Marks, Hopping transport in conductive heterocyclic oligomers: reorganization energies and substituent effects, *J. Am. Chem. Soc.*, 2005, **127**(7), 2339–2350.
37 R. A. Marcus, Chemical and electrochemical electron-transfer theory, *Annu. Rev. Phys. Chem.*, 1964, **15**(1), 155–196.
38 A.-J. Payne, J. S. McCahill and G. C. Welch, Indoloquinoxaline as a terminal building block for the construction of π-conjugated small molecules relevant to organic electronics, *Dyes Pigm.*, 2015, **123**, 139–146.
39 J.-L. Brédas, J. E. Norton, J. Cornil and V. Coropceanu, Molecular understanding of organic solar cells: the challenges, *Acc. Chem. Res.*, 2009, **42**(11), 1691–1699.
40 J. E. Coughlin, Z. B. Henson, G. C. Welch and G. C. Bazan, Design and synthesis of molecular donors for solution-processed high-efficiency organic solar cells, *Acc. Chem. Res.*, 2014, **47**(1), 257–270.
41 X. Zou, G. Wen, R. Hu, G. Dong, C. Zhang, W. Zhang, H. Huang and W. Dang, An insight into the excitation states of small molecular semiconductor Y6, *Molecules*, 2020, **25**(18), 4118.
42 C. Yan, S. Barlow, Z. Wang, H. Yan, A. K.-Y. Jen, S. R. Marder and X. Zhan, Non-fullerene acceptors for organic solar cells, *Nat. Rev. Mater.*, 2018, **3**(3), 1–19.
43 W. Akram, A. Walayat, W. A. Zahid, G. S. Khan, M. M. Alanazi, A. Elmushyakhi and J. Iqbal, Rational design and engineering of terminal functional groups in dibenzothiophene-diphenylamine small molecular electron donors for enhanced photovoltaic efficiency in all-small-molecule organic solar cells, *Adv. Theory Simul.*, 2024, **7**(8), 2400289.
44 R. Zaier, A. Martel and T. J. Antosiewicz, Effect of benzothiadiazole-based π-spacers on fine-tuning of optoelectronic properties of oligothiophene-core donor materials for efficient organic solar cells: a DFT study, *J. Phys. Chem. A*, 2023, **127**(50), 10555–10569.

45 P. Murugan, T. Hu, X. Hu and Y. Chen, Advancements in organic small molecule hole-transporting materials for perovskite solar cells: past and future, *J. Mater. Chem. A*, 2022, **10**(10), 5044–5081.
46 C. Ceriani, F. Corsini, G. Mattioli, S. Mattiello, D. Testa, R. Po, C. Botta, G. Griffini and L. Beverina, Sustainable by design, large Stokes shift benzothiadiazole derivatives for efficient luminescent solar concentrators, *J. Mater. Chem. C*, 2021, **9**(41), 14815–14826.
47 A. Khasbaatar, Z. Xu, J.-H. Lee, G. Campillo-Alvarado, C. Hwang, B. N. Onusaitis and Y. Diao, From solution to thin film: molecular assembly of π-conjugated systems and impact on (opto) electronic properties, *Chem. Rev.*, 2023, **123**(13), 8395–8487.
48 G. Han and Y. Yi, Origin of photocurrent and voltage losses in organic solar cells, *Adv. Theory Simul.*, 2019, **2**(8), 1900067.
49 S. M. Menke, N. A. Ran, G. C. Bazan and R. H. Friend, Understanding energy loss in organic solar cells: toward a new efficiency regime, *Joule*, 2018, **2**(1), 25–35.
50 K. Pei, Y. Wu, A. Islam, Q. Zhang, L. Han, H. Tian and W. Zhu, Constructing high-efficiency D–A–π–A-featured solar cell sensitizers: a promising building block of 2,3-diphenylquinoxaline for antiaggregation and photostability, *ACS Appl. Mater. Interfaces*, 2013, **5**(11), 4986–4995.
51 S. Li, W. Li and J. Ma, Generalized energy-based fragmentation approach and its applications to macromolecules and molecular aggregates, *Acc. Chem. Res.*, 2014, **47**(9), 2712–2720.
52 N. Wei, Y. Guo, H. Song, Y. Liu, H. Lu and Z. Bo, Reducing non-radiative energy losses in non-fullerene organic solar cells, *ChemSusChem*, 2025, **18**(6), e202402169.
53 M. Madhu, R. Ramakrishnan, V. Vijay and M. Hariharan, Free charge carriers in homo-sorted π-stacks of donor–acceptor conjugates, *Chem. Rev.*, 2021, **121**(13), 8234–8284.
54 K. N. Zhang, X. Y. Du, L. Yan, Y. J. Pu, K. Tajima, X. Wang and X. T. Hao, Organic photovoltaic stability: understanding the role of engineering exciton and charge carrier dynamics from recent progress, *Small Methods*, 2024, **8**(2), 2300397.
55 H. B. Naveed, K. Zhou and W. Ma, Interfacial and bulk nanostructures control loss of charges in organic solar cells, *Acc. Chem. Res.*, 2019, **52**(10), 2904–2915.
56 G. Han, Y. Yi and Z. Shuai, From molecular packing structures to electronic processes: theoretical simulations for organic solar cells, *Adv. Energy Mater.*, 2018, **8**(28), 1702743.
57 X. Kong, T. He, H. Qiu, L. Zhan and S. Yin, Progress in organic photovoltaics based on green solvents: from solubility enhancement to morphology optimization, *Chem. Commun.*, 2023, **59**(81), 12051–12064.
58 J. Han, H. Xu, S. H. K. Paleti, A. Sharma and D. Baran, Understanding photochemical degradation mechanisms in photoactive layer materials for organic solar cells, *Chem. Soc. Rev.*, 2024, **53**(14), 7426–7454.
59 J.-L. Lan, X.-N. Liu, C.-N. Xiao, M.-Y. Sui and G.-Y. Sun, Correction of the calculation method of CT state energy in ITIC and Y6 acceptor systems, *J. Photochem. Photobiol., A*, 2024, **456**, 115821.
60 J. Yang, X. Wu, Q.-S. Li and Z.-S. Li, Boron-based non-fullerene small molecule acceptors via nitrogen substitution: a theoretical study, *Mater. Adv.*, 2022, **3**(7), 3229–3237.